Heliyon 10 (2024) e27432

Contents lists available at ScienceDirect

Heliyon

journal homepage: www.cell.com/heliyon

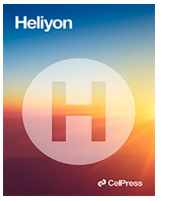

Research article

A deep learning classification task for brain navigation in rodents using micro-Doppler ultrasound imaging

Théo Lambert [a,b,c,d], Clément Brunner [a,b,c,d], Dries Kil [a,b,c,d], Roel Wuyts [c], Ellie D'Hondt [c], Gabriel Montaldo [a,b,c,d], Alan Urban [a,b,c,d,*]

[a] Neuro-Electronics Research Flanders, Leuven, Belgium
[b] VIB, Leuven, Belgium
[c] Imec, Leuven, Belgium
[d] Department of Neuroscience, Faculty of Medicine, KU Leuven, Leuven, Belgium

ARTICLE INFO

Keywords:
Brain-wide ultrasound imaging
Micro-Doppler imaging
Convolutional neural networks neuro-positioning and navigation

ABSTRACT

Positioning and navigation are essential components of neuroimaging as they improve the quality and reliability of data acquisition, leading to advances in diagnosis, treatment outcomes, and fundamental understanding of the brain. Functional ultrasound imaging is an emerging technology providing high-resolution images of the brain vasculature, allowing for the monitoring of brain activity. However, as the technology is relatively new, there is no standardized tool for inferring the position in the brain from the vascular images. In this study, we present a deep learning-based framework designed to address this challenge. Our approach uses an image classification task coupled with a regression on the resulting probabilities to determine the position of a single image. To evaluate its performance, we conducted experiments using a dataset of 51 rat brain scans. The training positions were extracted at intervals of 375 μm, resulting in a positioning error of 176 μm. Further GradCAM analysis revealed that the predictions were primarily driven by subcortical vascular structures. Finally, we assessed the robustness of our method in a cortical stroke where the brain vasculature is severely impaired. Remarkably, no specific increase in the number of misclassifications was observed, confirming the method's reliability in challenging conditions. Overall, our framework provides accurate and flexible positioning, not relying on a pre-registered reference but rather on conserved vascular patterns.

1. Introduction

Advances in medical imaging over the past decades have largely changed clinical practice. In particular, the advent of image-guided neurosurgery has significantly improved patient outcomes by allowing the accurate identification of critical areas and trajectory estimation for the surgical procedure [1,2]. An essential aspect of neuro-navigation systems is their ability to match intra-operative positions to pre-operative images, called registration process [3,4].

Likewise, preclinical research has benefited greatly from the development of neuroimaging technologies and faces similar requirements in terms of positioning. Indeed, for interpreting the data or targeting specific regions, scientists use references typically defined by the cellular structure of the brain, e.g. in the Allen [5] and Paxinos [6] atlases for rodents. Accurate localization and

* Corresponding author. Neuro-Electronics Research Flanders, Leuven, Belgium.
E-mail address: alan.urban@nerf.be (A. Urban).

https://doi.org/10.1016/j.heliyon.2024.e27432
Received 15 June 2023; Received in revised form 28 February 2024; Accepted 28 February 2024
Available online 6 March 2024

registration of the recorded data is therefore critical. As a consequence, specific software packages have been developed for different imaging modalities [7–11] and inter-experiments alignment [12].

Applied in both preclinical (e.g., rodent [13–16], bird [17], ferret [18] and non-human primate [19,20]) and clinical contexts (e.g., neonates [21,22] and adults [23,24]), functional ultrasound (fUS) imaging is a breakthrough technology combining large depth-of-field and high spatiotemporal resolution [25–27]. By repeating the acquisition of micro-Doppler images over time, fUS tracks the hemodynamics of brain vessels [13,25,28,29] reflecting changes in neuronal activity [15,30–33]. Nonetheless, a micro-Doppler image does not provide the morphological information generally used by other modalities for registration, as the correspondence between cerebro-vasculature and anatomy is only partial.

Manual registration of micro-Doppler images is typically performed by matching landmarks (e.g., cortical surface, major brain regions and vessels) with a reference atlas [27,34]. Performing the precise localization of single images with this process is challenging as it does not fully account for morphological variability across individuals or models [35,36]. Furthermore, this approach is time consuming and subject to inter-operator variability. Therefore, there is a strong need for a positioning system accurately inferring anatomical positions from the conserved brain vasculature [37–39].

An automated methodology has recently been proposed for ultrasound-based neuro-navigation on mice [40]. It relies on the online registration of a micro-Doppler scan acquired at the beginning of every experiment to a reference micro-Doppler volume pre-registered to an atlas. Yet, the registration is sensitive to inter-animal variability and the initial brain scan makes the approach not compatible with all experimental contexts. This includes for instance small imaging windows and larger brains where only a limited portion is imaged.

To circumvent these limitations, we designed a deep learning-based framework leveraging convolutional neural networks (CNN) to predict the anatomical position of input micro-Doppler images. We propose to train a model to classify input images into a fixed set of positions evenly distributed across the brain. Resulting probability distribution are further used to regress the location of single micro-Doppler images with 176 μm precision. Solely based on the brain vasculature, this strategy is reliable, reference-free, and user-independent.

2. Materials and Methods

2.1. Animals

Experimental procedures were approved by the Committee on Animal Care of the Catholic University of Leuven, in accordance with the national guidelines on the use of laboratory animals and the European Union Directive for animal experiments (2010/63/EU). Adult male Sprague-Dawley rats (n = 51; Janvier Labs, France) with an initial weight between 200 and 300 g were housed in standard ventilated cages and kept in a 12 : 12 h reverse dark/light cycle environment at a temperature of 22 °C with *ad libitum* access to food and water.

2.2. Cranial window for brain-wide imaging and stroke induction

The entire procedure for animal preparation and imaging is performed under isoflurane anesthesia (Iso-Vet, Dechra, Belgium). A mixture of 5% isoflurane in compressed dry air was used to induce anesthesia, subsequently reduced to 2.0–2.5% during surgery, and to 1.5% for imaging (see Brunner et al. [41] for details on surgical procedure). Xylocaine (0.5%, AstraZeneca, England) and Metacam (0.2 mg/kg, Boehringer Ingelheim, Canada) were injected subcutaneously as pre-operative and post-operative analgesia; respectively. Intraperitoneal injection of 5% glucose solution was provided every 2 h to prevent dehydration. The cranial window extended from Bregma +4.0 to −7.0 mm antero-posterior, laterally ±6.0 mm was performed in all rats. 26 rats were subjected to stroke by the mean of permanent occlusion of the distal branch of the left middle cerebral artery as detailed in Brunner et al. [41].

2.3. Micro-Doppler ultrasound imaging of brain vasculature

The data acquisition was performed using an ultrasound imaging scanner equipped with custom acquisition and processing software described in Ref. [27]. The scanner is composed of a linear ultrasonic transducer (15 MHz, 128 elements, Xtech15, Vermon, France) connected to 128 channel emission-reception electronics (Vantage, Verasonics, USA) controlled by a high-performance computing workstation (fUSI-2, AUTC, Estonia). The transducer was fixed to a fine resolution motorized linear stage (T-LSM200A, Zaber Technologies Inc., Canada) allowing for the precise postero-anterior scanning of the brain. The acoustic coupling between the brain and the probe is ensured by a layer of agarose and ultrasound gel (Aquasonic Clear, Parker Laboratories Inc, USA). Each coronal Doppler image is 12.8 mm width and 9 mm depth and is composed of 300 compound images acquired at 500 Hz. Each compound image is computed by adding nine plane-wave (4.5 kHz) with angles from −12° to 12° with a 3° step. The blood signal was extracted from 300 compound images using a single value decomposition filter and removing the 30 first singular vectors [42]. The micro-Doppler image is computed as the mean intensity of the blood signal in these 300 frames that is an estimator of the cerebral blood volume [13,25]. This sequence enables a temporal resolution of 0.6 s, an in-plane resolution of 100 × 110 μm, and an off-plane (thickness of the image) of 300 μm[27]. Using these parameters, a scan of the brain vasculature consisting of 89 coronal images of size 183 × 128 pixels and spaced by 125 μm was performed between Bregma −6.5 to +3.0 mm.

2.4. Registration of micro-Doppler images

The micro-Doppler 2D scans from all animals were aligned along the antero-posterior axis with respect to recognizable anatomical and vascular patterns (Fig. 1-c). This alignment is necessary for correcting potential shifts occurring either during surgery, imaging or due to inter-animal variability. The process was performed independently by two experts, and any disagreement was resolved post-hoc by consensus. Such alignment resulted in 77 common positions across animals. Each micro-Doppler image is then identified by its anatomical position with respect to the Bregma reference point, e.g., Bregma −3.0 mm.

2.5. Down-sampled datasets generation

Several datasets have been extracted from the initial scans using a down-sampling factor ranging from 2 to 5. This corresponds to an artificial increase in the spacing between two consecutive micro-Doppler images. To create the dataset associated with a given factor F, we extracted images from Bregma −3.0 mm with a spacing of Fx125 μm within the limits of the cranial windows, yielding a subset of common positions. The 5 datasets spaced by [250, 375, 500, 625, 750] μm, respectively contain [39, 26, 20, 15, 13] different positions. 50% of the animals were randomly selected for training, 25% for tuning the hyperparameters (i.e., validation) and the remaining 25% for evaluating the final performances of the model (i.e., test).

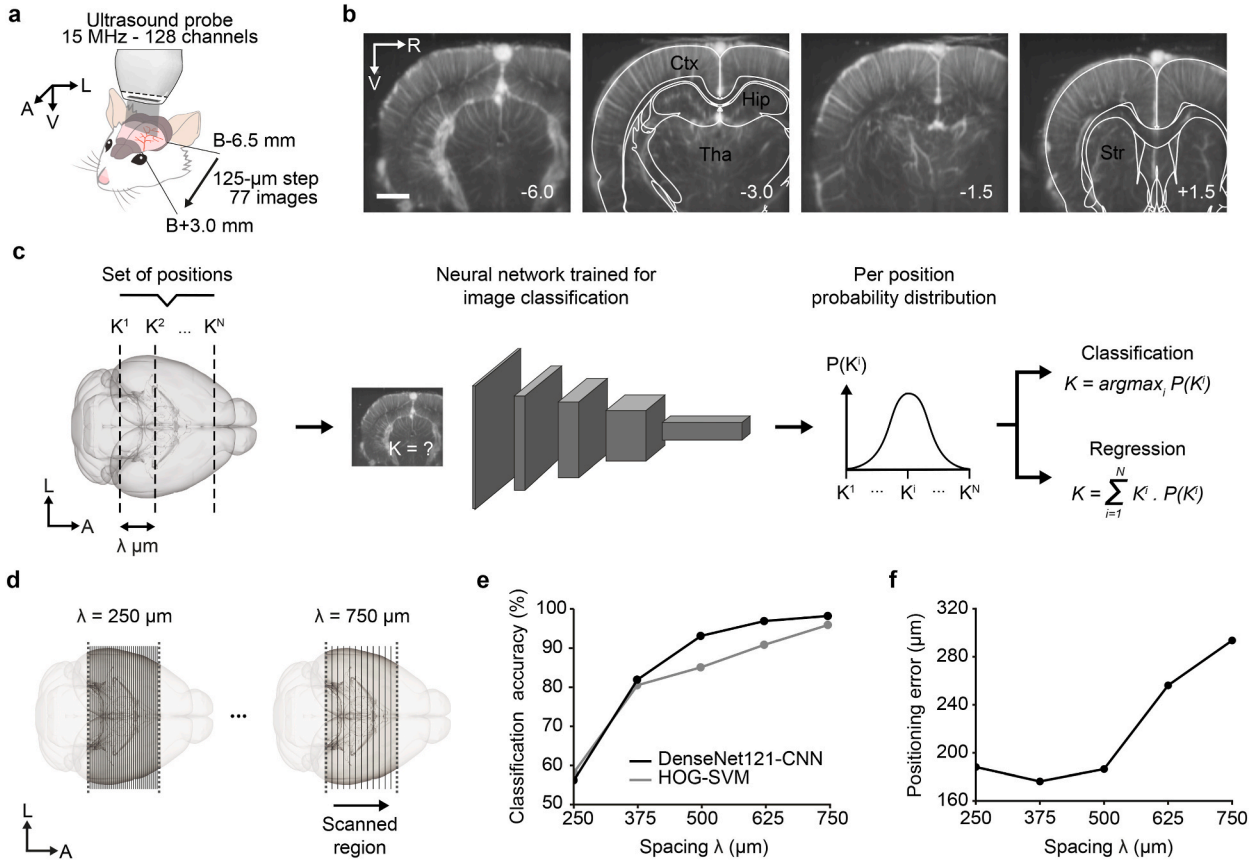

Fig. 1. Methodological approach and spacing selection. **a-** Acquisition setup for large-scale micro-Doppler imaging of rat brains. The ultrasonic probe is moved along the postero-anterior axis using a motorized linear stage. The imaging was performed from Bregma −6.5 to +3.0 mm with a 125 μm spacing for a total number of 89 images. **b-** Set of micro-Doppler images extracted from a single scan overlaid with a simplified version of the Paxinos brain atlas [6] in white. Main anatomical structures are identified in black: Cortex (Ctx), Hippocampus (Hip), Thalamus (Tha), Striatum (Str). The Bregma position (in mm) of the micro-Doppler images is shown in the lower right corner. Scale bar: 2 mm. **c-** Schematic representation of the position inference procedure. Left: a set of positions (K^1, …, K^N) with spacing λ μm is defined over the brain. Center: an image with unknown position K is fed to a neural network trained to classify input micro-Doppler images depending on their position. Right: the network output a probability distribution over the positions (K^1, …, K^N). It can be used either to determine K as being the most likely position within (K^1, …, K^N) (classification), or to estimate K as a weighted sum of all positions using their respective probabilities (regression). **d-** Down-sampling procedure used to determine an optimal set of positions. Each scan is down-sampled using 5 factors, corresponding to an increase in the spacing λ between two consecutive images: 250, 375, 500, 625 and 750 μm. **e-** Classification accuracy (%) of DenseNet121-CNN (black) and HOG-SVM (grey) models for each spacing (testing, n = 13 rats). **f-** Regression error (μm) obtained from the DenseNet121-CNN model for each spacing (testing, n = 13 rats). A: anterior, L: left, R: right, V: ventral.

2.6. Image preprocessing

To equalize the contrast value distributions, a correction factor (power of 0.25) has been applied to every pixel of all images in each dataset. The intensity amplitude was then normalized to fit into a [0, 1] interval. The overall process has been implemented using MATLAB (R2018b, Mathworks, USA).

2.7. Positioning methodology

Our design is composed of a neural network classifier followed by a linear regression for predicting the anatomical position of input micro-Doppler images. Due to the technology's off-plane resolution of 300 μm, a predefined set of positions is used to avoid or minimize information overlap during training. However, this limits the positions that can be inferred to the predefined set. To circumvent this issue, we added a linear regression stage leveraging the probability distributions learned during the classification to infer locations between predefined positions.

2.8. Model selection

To select the optimal classifier for the experiments, we evaluated 5 convolutional neural network architectures (CNN; ResNet50 [43], DenseNet121 [44], VGG11 [45], ViT-Base-16 [46] and EfficientNetV2-S[47]), and support vector machines (SVM) with different feature extraction methods (HOG [48], SIFT [49], PCA) and kernels [50]. These models were selected for their compatibility with datasets of relatively small sample sizes. Both ResNet50-CNN and DenseNet121-CNN were pretrained on ImageNet [51] as previously suggested [52]. The default parameters and architectures were used, as implemented in the 'torchvision' (PyTorch, version 0.7.0) Python package. The last layer of the network - the classifier - was replaced by a fully connected layer outputting n values, n being the number of positions in the training set and passed through a softmax layer afterwards. Both CNN and SVM models were trained and evaluated on the dataset with 375 μm spacing, corresponding to the smallest spacing above the antero-posterior spatial resolution of the modality employed. It therefore corresponds to the largest dataset without overlapping information. SVMs were implemented using the 'scikit-learn' (version 0.23.1) Python package.

Training and evaluation procedures for CNNs.

For each of the datasets used in this work, images were resized to 224 × 320 pixels by bicubic interpolation, and their grey channel extended in RGB to fit the ImageNet format imposed by the pre-training [51]. All the data were normalized with the mean and standard deviation of the full dataset. We augmented the size of the training set with rotations of ±4°and ±8° applied to all micro-Doppler images. The significance of such process was validated through an ablation study, resulting in lower accuracy but with no statistically significant difference (79.6 versus 81.9 %, $p = 0.322$, McNemar test). The weights of the network were optimized with the Adam algorithm using a cross-entropy loss function. The hyperparameters were selected through a random search (see Supplementary Tables S3 and S4). Other parameters were kept with default values. The final model performance was then evaluated on the testing set. The overall procedure has been performed on a single machine, equipped with Xeon E5-2620 CPU (Intel, USA), 64 Gb RAM and 4 RTX2080 (8 Gb) GPUs (Nvidia, USA).

2.9. Probability-based regression and positioning error calculation

This step occurs after the training of the model for the classification task. When an input image is fed to the network, it outputs a probability $P(K_i)$ for each one of the positions $(K_i)_{1\leq i\leq N}$ included in the training set. We use these probabilities to obtain an estimate $\widehat{K}$ of the position K using the following equation:

$$\widehat{K} = \sum_{i=1}^{N} K_i \,.\, P(K_i)$$

The positioning error is defined as $\sigma(K - \widehat{K})$, where σ denotes the standard deviation.

2.10. Visualization of relevant features for image classification using GradCAM

We extracted the pixels in the input image driving the classification using the Gradient-weighted Class Activation Map (GradCAM) technique, following the recommendations Adebayo et al. [53] on the relevant visualization approaches. This method aggregates the gradients associated with the prediction for each feature map in a given layer, to produce a coefficient measuring the contribution of each of the map to the network's prediction. Here, the gradients and feature maps were extracted at the last layer before the classifier. The output heatmaps were then resized by bilinear interpolation to the original image and a threshold at 0.7 was applied to limit the effect of the interpolation.

2.11. GradCAM registration on atlas for anatomical extraction

We used a digital version of the rat brain Paxinos atlas [6,34] to extract the anatomical regions associated with the GradCAM heatmaps. The input scan was taken as a volume and interpolated to fit the atlas resolution (50 × 50 × 50 μm^3 voxel size). A 3D rigid

registration was performed using a MATLAB custom script [27,41]. This procedure has been applied to all the samples from the validation and testing sets by an expert. To extract the regions from the GradCAM heatmap, a volume (89 planes as the input data) was constructed from the heatmaps by zero-padding the missing sections before applying the transformation matrix.

2.12. Evaluation on the stroke dataset

We used 26 rats subjected to stroke (see above and ref. [41]). All rats were imaged in the original dataset, and 14/7/7 individuals were respectively present in training/validation/testing sets. The scans were registered and a dataset with 375 μm spacing was created following the same procedure as for the previous experiment. The classes predictions were obtained by processing the images through the DenseNet121-CNN previously trained on the pre-stroke dataset with 375 μm spacing, without re-training.

3. Results

3.1. Operating principle

Our method uses a neural network trained on a classification task to find the position of a given image. Three main elements are required for the implementation: 1) an input dataset of images aligned with respect to a predefined reference, 2) a neural network trained to classify images depending on their position, and 3) a probability-based regression that infers the position of a new input image. These parts are detailed below in the context of rat brains and with a DenseNet121-CNN. However, it is important to note that this operating principle is not species- nor neural network-specific.

1) Input dataset

In this study we used a set of 51 rat brains. Each brain was scanned with 77 micro-Doppler images extending from Bregma +3.0 to −6.5 mm with an in-between image spacing of 125 μm (Fig. 1-a). A micro-Doppler image has an in-plane resolution of 100 × 110 μm and 300 μm slice thickness in this setting [13,25,27]. Example micro-Doppler images on which major anatomical structures and vessels were annotated are shown in Fig. 1-b andSupplementary Fig. S1. Scans were aligned on reference positions by expert consensus (**Materials and Methods – Registration of micro-Doppler images**), allowing for associating each image with an anatomical position defined with respect to Bregma, e.g., Bregma −3.0 mm.

2) Neural network-based image classification

For the needs of this study, we constrained the selection to classical models. After a preliminary performance evaluation (Supplementary Table S1, **Materials and Methods – Model selection**), a DenseNet121-CNN and HOG-SVM with additive χ^2-kernel were selected as main and baseline models, respectively [44,48]. Both were trained to classify input micro-Doppler images with respect to their position on a subset of 25 rats, for a given set of positions (Fig. 1-c). The hyperparameters were tuned on a validation set of 13 rats, and their performance was assessed on a testing set of 13 rats.

3) Navigation stage

Given a new image with unknown position, the CNN outputs a probability for each position included in the training dataset. The training positions themselves are used as regressors and their probabilities as corresponding coefficients in a regression model, providing the actual position estimate (Fig. 1-c).

A block diagram providing an overview of the different elements of the model is provided inSupplementary Fig. S2. To assess the performance of our approach, we evaluated the accuracy of the classifier and the associated positioning error, analyzed their spatial dependence, and extracted the anatomical regions supporting the inference.

3.2. Effect of the scanning spacing in the input dataset

In order to determine a suitable spacing to scan the brains in the input dataset, we created five datasets by down-sampling the original brain scans at 250 μm (39 positions), 375 μm (26 positions), 500 μm (20 positions), 625 μm (15 positions) and 750 μm (13 positions) (Fig. 1-d).

Both DenseNet121-CNN and HOG-SVM show an increase in the classification accuracy along with the spacing (250–750 μm), from 56.2% to 98.2% and from 58% to 95.9%, respectively (Fig. 1-e andSupplementary Table S2). The training and validation accuracies follow similar trends, indicating that the models did not pathologically overfit training data (Supplementary Fig. S3). As an additional control, we performed a 5-fold cross-validation on the 375 μm dataset, which resulted in comparable testing accuracy (80.9 ± 2.3%). It should be noted that the CNN did not converge with 125 μm spacing.

The testing accuracy is lower for the HOG-SVM compared to the DenseNet121-CNN, irrespective of the spacing. However, the performance comparison using the McNemar [54] statistical test exhibited no statistically significant differences apart from spacings 500 and 625 μm (**p = 0.0012 and * p = 0.012, respectively;Supplementary Table S2). With regards to the extrema, both models achieve similar maximum class accuracy, while the DenseNet121-CNN provides respectively higher and lower minimum class

accuracy than the HOG-SVM for spacings 625/500 μm and 375/250 μm.

Although better for the classifier accuracy, increasing the spacing decreases the resolution of the positioning. To determine the value that gives the most accurate results, we estimated the positioning error. It is defined as the standard deviation of the differences between the predicted positions and the target positions in the animals of the validation set (Fig. 1-c, Materials and Methods – Probability-based regression and positioning error calculation). The 375 μm spacing dataset gave the best result with a regression error of 176 μm and was therefore selected for further investigation. For comparison purposes, we also computed the positioning error with the other CNN models (i.e., ResNet50, DenseNet121, VGG11, ViT-Base-16, and EfficientNetV2-S; seeSupplementary Table S1).

3.2.1. *Spatial dependency of the classification*

To assess the reliability of the inference in different parts of the brain, we examined the classification accuracies by position on the dataset with 375 μm spacing. The values are non-uniformly distributed and range from 30.8 to 100% (Fig. 2-a). The DenseNet121-CNN and HOG-SVM displayed similar results overall, and the anterior part of the brain generally elicited lower accuracies for both models (5 of the 8 positions with accuracy below the mean are between Bregma 0.0 to +3.0 mm). The DenseNet121-CNN-associated confusion matrix reveals that misclassified images were mapped to neighboring positions (Fig. 2-b) and were not concentrated in a subset of rats.

We then computed the positioning error per position for the DenseNet121-CNN model (Fig. 2 c, Materials and Methods – Probability-based regression). Although not fully proportional, the distribution of positioning errors closely matches the classification accuracies, especially with higher error in the anterior part of the brain.

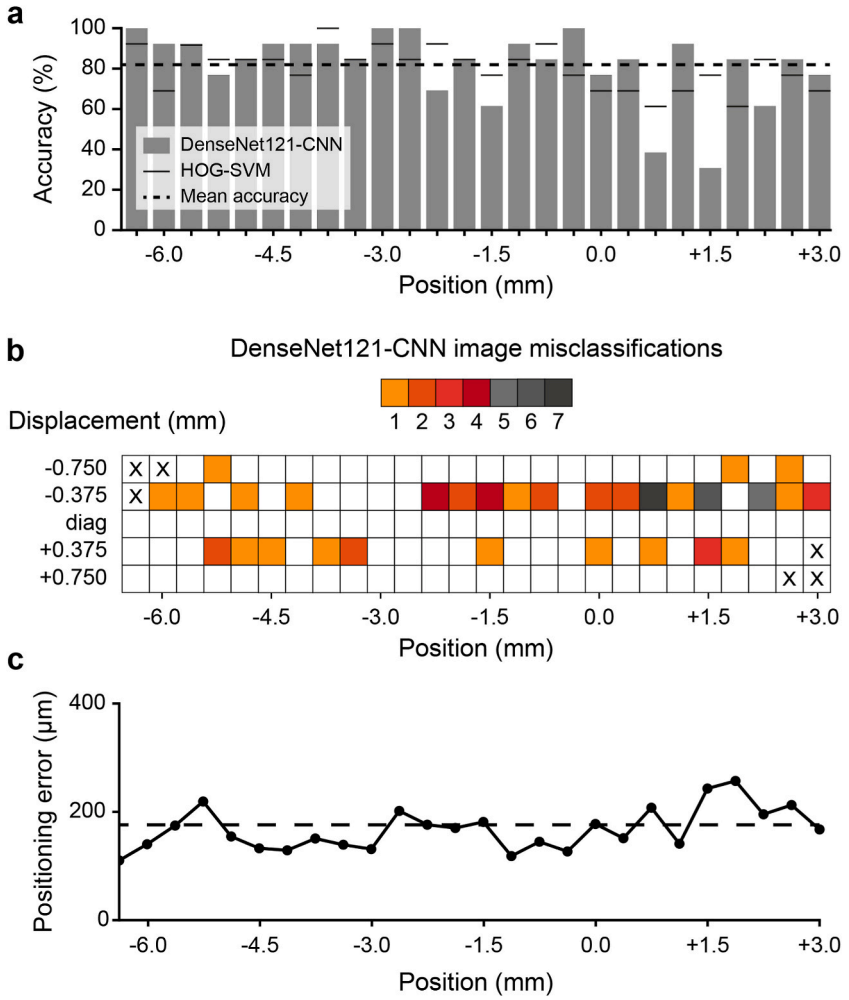

Fig. 2. Per position analysis of the DenseNet121-CNN predictions a- Per position display of the DenseNet121-CNN accuracies for the dataset with 375 μm spacing (testing, n = 13 rats). The horizontal dashed line represents the mean classification accuracy. For each position, the black dash represents the accuracy for the HOG-SVM model. **b-** Representation of the extended diagonal of the DenseNet121-CNN confusion matrix. Each arrow goes from the correct position towards the predicted position. The different colors represent the number of misclassified micro-Doppler images (375 μm spacing, testing, n = 13 rats). **c-** Distribution of positioning error with respect to the Bregma position (DenseNet121-CNN trained on 375 μm spacing dataset, testing, n = 13 rats).

3.2.2. Spatial localization of the discriminative patterns

To visualize the discriminative features underlying the accurate classification, we computed the gradient-weighted class activation maps (GradCAM) [55]. This visualization technique highlights the area of an image contributing the most to the network's inference of a given prediction. We registered the 2D scans with a digital version of the rat Paxinos atlas [6] (as previously done by Brunner et al. [41]) to i) adjust for potential differences in probe positioning and ii) allow for inter-animal comparison. For each position, the GradCAM results were averaged across animals and a threshold was applied to mitigate the effect of interpolating such low resolution heatmaps (Fig. 3-a).

The average maps were overlaid per position on the corresponding registered micro-Doppler images (Fig. 3-b). Interestingly, a single part of the micro-Doppler image is driving the classification regardless of the location in the brain, except for Bregma −2.625 and −1.875 mm exhibiting two small, connected areas. Furthermore, the GradCAM heatmaps are almost entirely located in the subcortex up to Bregma, where the proportion starts to decrease in favor of the cortex (Fig. 3-c). It corresponds to the general increase in the proportion of cortex in the image.

As the GradCAM maps appeared to be conserved across rats, we identified the associated local brain vasculature. It revealed that several branches of large vessels play a major role in the classification process. Most of these vessels supply brain regions located in subcortical regions, such as the thalamus, the hippocampus and the striatum [37,38], as shown in Fig. 1-b, Fig. 3-c and Supplementary Fig. S1.

Specifically, the most important vessels in the classification of the posterior part (Bregma −6.375 to 0.0 mm) include the thalamoperforating arteries branching from the posterior cerebral artery (PCA), the thalamostriate veins and branches (tlv), and the patterns created by adjacent vessels such as the great cerebral vein of Galen (GcvG) and the longitudinal hippocampal veins (lhv). The classification of the anterior part (Bregma 0.0 to +3.0 mm) mostly relies on the anterior cerebral artery (ACA), the azygos pericallosal arteries (APCA) and the thalamostriate veins/arteries.

3.3. Model robustness evaluation on a cortical stroke model

To further validate the reliability of the highlighted subcortical vascular patterns and the robustness to pathological condition, we assessed the performance of the DenseNet121-CNN on a cortical stroke model. From the 51 rats of the input dataset, a subset of 26 rats were subjected to cortical stroke by means of the permanent occlusion of the left middle cerebral artery (MCA) distal branch, provoking a significant decrease of signal (−60%) in the cortex of the left hemisphere. Brain-wide micro-Doppler scans were acquired after stroke onset (top and bottom row, respectively; Fig. 4-a). More details about the experimental procedure and quantification are

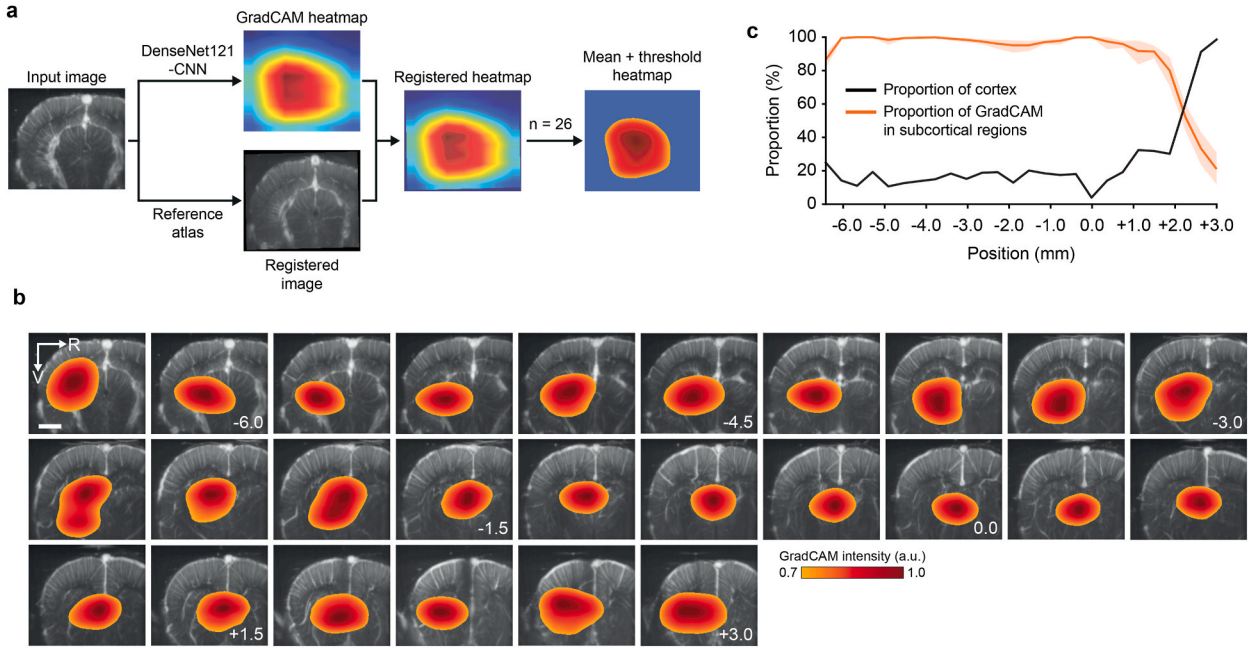

Fig. 3. Visualization of the predictions using Gradient-weighted Class Activation Map (GradCAM). **a-** Workflow for generating the average GradCAM heatmap. Each image is processed through the DenseNet121-CNN model to collect the GradCAM heatmaps and is registered in parallel for in-plane alignment. The 26 heatmaps, including validation and testing sets, are averaged and a threshold at 0.7 is applied. **b-** Averaged GradCAM heatmaps overlaid on corresponding (registered) micro-Doppler images. The color scale indicates the GradCAM intensity (a.u., arbitrary unit). The Bregma position (in mm) of the micro-Doppler images is shown in the lower right corner. Scale bar: 2 mm. **c-** Proportion of the GradCAM heatmap located in subcortical regions (orange). The error band corresponds to the 95 % confidence interval. The black curve displays the reference proportion of cortex for each position.

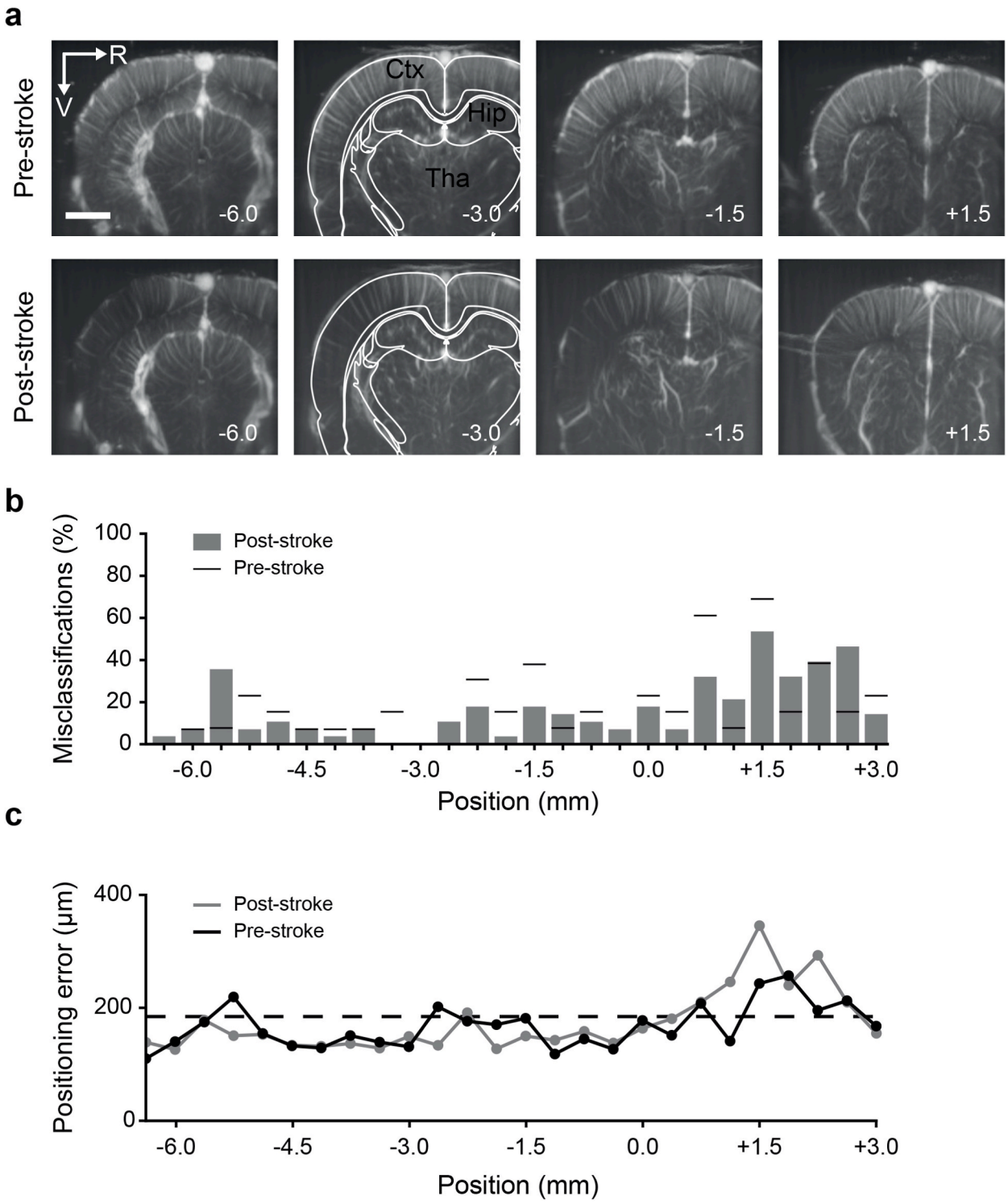

Fig. 4. Effect of a cortical stroke on the classification accuracy. **a-** Set of micro-Doppler images before (Pre-stroke - top row) and after stroke induction (Post-stroke- bottom row). A simplified version of the Paxinos atlas [6] is overlaid in white. Main anatomical structures are identified in black: Cortex (Ctx), Hippocampus (Hip), Thalamus (Tha). The position from Bregma (in mm) of the micro-Doppler images is shown in the lower right corner. Scale bar: 2 mm. **b-** Proportion of micro-Doppler images misclassified before (Pre-stroke, black dash) and after (Post-stroke, grey bar) the stroke induction at each position for DenseNet121-CNN (n = 26 rats). **c-** Distribution of positioning error with respect to the Bregma position before (black) and after (grey) stroke induction (DenseNet121-CNN trained on 375 µm spacing dataset, n = 26 rats).

available in Ref. [41]. It should be noted that the anterior positions are minimally affected by the signal loss because those territories are poorly supplied by the MCA [38].

The positions of the post-stroke images were predicted without prior retraining and the proportion of post-stroke misclassifications was computed. Images of animals originally present in the training, validation and testing sets were pooled for this experiment. Overall, 16.5% of the images were misclassified as compared to the 18.1% on the pre-stroke test set. Looking at the distribution of misclassifications per position, pre- and post-stroke exhibit similar results with only local variations (Fig. 4-b). Likewise, the regression error did not display significant post-stroke change in terms of average error (176 vs. 185 μm, respectively pre/post), with consistently higher positioning error from Bregma +0.0 mm (Fig. 4-c).

4. Discussion

In this study, we proposed a classification framework suited for accurate and robust brain positioning and neuro-navigation during fUS imaging. Our approach relies on a neural network-based image classification task to identify a set of training positions. This serve as a reference frame from which the location of a micro-Doppler image can be inferred with precision through a regression. We have selected a DenseNet121-CNN as main model and an HOG-SVM as baseline model, nevertheless the methodology is not neural network-specific and can therefore be applied with other architectures.

First, we have defined a set of anatomical reference positions that act as classes in our classification task. By analyzing the effect of differently spaced positions, we concluded that 375 μm provides an optimal positioning error of 176 μm. We computed the positioning errors with the other models that were included in the model selection process. ResNet50 and VGG11-CNN yielded worse results (~300 μm positioning error), while ViT-Base-16 and EfficientNetV2-S-CNN gave errors comparable to DenseNet121, thus demonstrating the framework's versatility.

As a result, the position of an unknown image can be determined with an error of 352 μm with 95 % confidence. This is consistent with the size of the micro-Doppler image thickness (~300 μm). Such 375 μm spacing is a trade-off between the resolution and the classification confidence: indeed, using a larger spacing allows more accurate classification but at the cost of less precision in inferring the final position. Conversely, a too small spacing has a detrimental effect on the overall positioning error, which can be attributed to the vascular similarity in adjacent planes when exceeding the technology resolution.

Further analysis using the GradCAM visualization technique revealed that the classification was mainly driven by highly consistent vascular structures located in subcortical regions. Since ImageNet pretraining is known to introduce a bias towards texture differences [56], the richer vascular texture of the subcortex may account for its prevalence compared to the cortex. This can also explain why the cortical curvature and thickness variation across anatomical locations are not essential in our approach.

Finally, we validated the CNN predictions in rats subjected to cortical stroke. The analysis revealed no significant differences in the number of misclassifications, except for local variations, thus confirming the robustness and reproducibility of the inference in challenging contexts.

Nevertheless, it should be noted that anterior positions in our datasets exhibited higher positioning errors following the stroke induction, while not being the most affected areas [41]. This observation further highlights the difficulty of performing accurate positioning anterior to Bregma +1.0 mm. This can be partially attributed to the similarity of the vascular patterns across positions in this area (cortical vessels, anterior cerebral artery and thalamoperforating vessels). To circumvent this issue, a first strategy could be to perform the positioning using a reference located farther away (e.g., before Bregma +1.0 or +3.0 mm), at the cost of a potentially wider cranial window. Another way could consist of leveraging super-resolution images obtained by the so-called Doppler slicing strategy [57] to search for clearer differences in vascular features across positions.

Overall, automated brain positioning and neuro-navigation with micro-Doppler images is an issue recently raised by new fUS users, but not yet widely investigated. To date, only one work has addressed the positioning problem through the automated registration of a micro-Doppler scan to a reference [40]. Our approach offers more flexibility as a single image is sufficient to find a position, while CNNs are fast enough for real-time implementation in the neuro-navigation context.

These benefits come at the cost of a need for large datasets to train the classifier. For this proof-of-concept study, we used a rather standardized dataset with limited data augmentation and validated the performance on a stroke dataset. Yet, datasets comprising more subjects as well as more variability (transducer orientation and position, different animal preparation and imaging sequences, further data augmentation, …) will be required to build a model suitable for routine use. In this regard, the increasing adoption of the fUS technology by the neuroscience community will facilitate the construction of large databases, especially for mice, the leading mammalian model.

Although our work is validated on anesthetized rats, our strategy is directly applicable to awake imaging and is not conceptually limited to rodents. Micro-Doppler imaging has been successfully applied to humans in neurosurgery [23,58,59] and non-invasively in newborns by imaging through the fontanel [21,22]. For such clinical applications where accurate positioning is critical, further research will be needed to address the challenges posed by the limited imaging depth and large differences in vessel scale.

5. Conclusion

This work presents an accurate all-ultrasound navigation strategy that can be customized for various experimental contexts. The approach combines a neural network-based classification task with regression to predict the position of single micro-Doppler images with an error of 176 μm. Although the preclinical study involved a large number of animals, the dataset size is still small compared to deep learning standards. To further refine the method, more samples and variability will be required. Future work should focus on

extending this strategy to 3D positioning with other transducer orientations, such as sagittal, and larger animal models to enable navigation in human brains.

Data availability statement

The data supporting the conclusions of this article will be made available by the authors, upon reasonable request.

Ethics statement

Experimental procedures on animals were approved by the Committee on Animal Care of the Catholic University of Leuven (protocol number 096/2017), in accordance with the national guidelines on the use of laboratory animals and the European Union Directive for animal experiments (2010/63/EU).

CRediT authorship contribution statement

Théo Lambert: Writing – original draft, Visualization, Validation, Software, Methodology, Formal analysis, Data curation, Conceptualization. **Clément Brunner:** Writing – review & editing, Visualization, Validation, Resources, Data curation. **Dries Kil:** Writing – review & editing, Validation. **Roel Wuyts:** Writing – review & editing, Validation, Funding acquisition. **Ellie D'Hondt:** Writing – review & editing, Supervision, Project administration, Funding acquisition. **Gabriel Montaldo:** Writing – review & editing, Writing – original draft, Supervision, Resources, Project administration, Methodology. **Alan Urban:** Writing – review & editing, Writing – original draft, Validation, Supervision, Project administration, Methodology, Formal analysis, Conceptualization.

Declaration of competing interest

The authors of this publication declare that they have no financial or non-financial conflicts of interest to disclose.

Acknowledgements

This work was supported by grants from IMEC PhD Talent grant for Théo Lambert, Fonds Wetenschappelijk Onderzoek (G0C9923N); Fonds Wetenschappelik Onderzoek (G079623N); Fonds Wetenschappelijk Onderzoek (12D7523N); ERANET, EU Horizon 2020 (Grant number 964215, UnscrAMBLY); HORIZON-MSCA-2022-DN-01 (Project 101119916 — SOPRANI). This research also received funding from IMEC and the Flemish regional government (AI Research Program). We thank the NERF animal caretakers including I. Eyckmans, F. Ooms, and S. Luijten, for their help managing the animals. We extend our gratitude to Dr. Matthew Blaschko and Dr. Johan Suykens for their valuable input on the manuscript and overall guidance in overseeing Théo Lambert's Ph.D. training.

Appendix A. Supplementary data

Supplementary data to this article can be found online at https://doi.org/10.1016/j.heliyon.2024.e27432.

References

[1] Y. Enchev, Neuronavigation: geneology, reality, and prospects, Neurosurg. Focus 27 (2009) E11.
[2] N.W.D. Thomas, Sinclair, J. Image-guided neurosurgery: history and current clinical applications, J. Med. Imag. Radiat. Sci. 46 (2015) 331–342.
[3] M.N. Wang, Z.J. Song, Classification and analysis of the errors in neuronavigation, Neurosurgery 68 (2011) 1131–1143. ; discussion 1143.
[4] F. Alam, S.U. Rahman, S. Ullah, K. Gulati, Medical image registration in image guided surgery: issues, challenges and research opportunities, Biocybern. Biomed. Eng. 38 (2018) 71–89.
[5] Q. Wang, et al., The Allen mouse brain common coordinate framework: a 3D reference atlas, Cell 181 (2020) 936–953.e20.
[6] G. Paxinos, C. Watson, Rat Brain in Stereotaxic Coordinates, Academic Press, 2007.
[7] C.J. Niedworok, et al., aMAP is a validated pipeline for registration and segmentation of high-resolution mouse brain data, Nat. Commun. 7 (2016) 11879.
[8] J.G. Fuglstad, P. Saldanha, J. Paglia, J.R. Whitlock, HERBS: histological E-data registration in rodent brain spaces, bioRxiv (2021), https://doi.org/10.1101/2021.10.01.462770.
[9] D. Xiao, B.J. Forys, M.P. Vanni, T.H. Murphy, MesoNet allows automated scaling and segmentation of mouse mesoscale cortical maps using machine learning, Nat. Commun. 12 (2021) 5992.
[10] L. Qu, et al., Cross-modal coherent registration of whole mouse brains, Nat. Methods 19 (2022) 111–118.
[11] J.S. Montijn, J.A. Heimel, A universal pipeline for the alignment of electrode tracks with slice histology and electrophysiological data, bioRxiv (2022), https://doi.org/10.1101/2022.06.20.496782.
[12] A. Giovannucci, et al., CaImAn an open source tool for scalable calcium imaging data analysis, Elife 8 (2019).
[13] E. Macé, et al., Functional ultrasound imaging of the brain, Nat. Methods 8 (2011) 662–664.
[14] A. Urban, et al., Real-time imaging of brain activity in freely moving rats using functional ultrasound, Nat. Methods 12 (2015) 873–878.
[15] É. Macé, et al., Whole-brain functional ultrasound imaging reveals brain modules for visuomotor integration, Neuron 100 (2018) 1241–1251.e7.
[16] C. Brunner, et al., A platform for brain-wide volumetric functional ultrasound imaging and analysis of circuit dynamics in awake mice, Neuron 108 (2020) 861–875.e7.
[17] R. Rau, et al., 3D functional ultrasound imaging of pigeons, Neuroimage 183 (2018) 469–477.
[18] C. Bimbard, et al., Multi-scale mapping along the auditory hierarchy using high-resolution functional UltraSound in the awake ferret, Elife 7 (2018).

[19] A. Dizeux, et al., Functional ultrasound imaging of the brain reveals propagation of task-related brain activity in behaving primates, Nat. Commun. 10 (2019) 1400.
[20] D.Y. Takahashi, et al., Social-vocal brain networks in a non-human primate, bioRxiv (2021), https://doi.org/10.1101/2021.12.01.470701.
[21] C. Demene, et al., Functional ultrasound imaging of the brain activity in human neonates, in: 2016 IEEE International Ultrasonics Symposium (IUS), IEEE, 2016, https://doi.org/10.1109/ultsym.2016.7728657.
[22] C. Demene, et al., Functional ultrasound imaging of brain activity in human newborns, Sci. Transl. Med. 9 (2017).
[23] S. Soloukey, et al., Functional ultrasound (fUS) during awake brain surgery: the clinical potential of intra-operative functional and vascular brain mapping, Front. Neurosci. 13 (2020).
[24] S. Soloukey, et al., High-resolution micro-Doppler imaging during neurosurgical resection of an arteriovenous malformation: illustrative case, J Neurosurg Case Lessons 4 (2022).
[25] E. Mace, et al., Functional ultrasound imaging of the brain: theory and basic principles, IEEE Trans. Ultrason. Ferroelectrics Freq. Control 60 (2013) 492–506.
[26] G. Montaldo, A. Urban, E. Macé, Functional ultrasound neuroimaging, Annu. Rev. Neurosci. 45 (2022) 491–513.
[27] C. Brunner, et al., Whole-brain functional ultrasound imaging in awake head-fixed mice, Nat. Protoc. 16 (2021) 3547–3571.
[28] J. Bercoff, et al., Ultrafast compound Doppler imaging: providing full blood flow characterization, IEEE Trans. Ultrason. Ferroelectrics Freq. Control 58 (2011) 134–147.
[29] C. Brunner, E. Macé, G. Montaldo, A. Urban, Quantitative hemodynamic measurements in cortical vessels using functional ultrasound imaging, Front. Neurosci. 16 (2022) 831650.
[30] A. Urban, et al., Chronic assessment of cerebral hemodynamics during rat forepaw electrical stimulation using functional ultrasound imaging, Neuroimage 101 (2014) 138–149.
[31] A. Sans-Dublanc, et al., Optogenetic fUSI for brain-wide mapping of neural activity mediating collicular-dependent behaviors, Neuron 109 (2021) 1888–1905.e10.
[32] A.O. Nunez-Elizalde, et al., Neural correlates of blood flow measured by ultrasound, Neuron 110 (2022) 1631–1640.e4.
[33] L.-A. Sieu, et al., EEG and functional ultrasound imaging in mobile rats, Nat. Methods 12 (2015) 831–834.
[34] C. Brunner, et al., Brain-wide continuous functional ultrasound imaging for real-time monitoring of hemodynamics during ischemic stroke, J. Cerebr. Blood Flow Metabol. 44 (1) (2024) 6–18.
[35] J.T. Richtsmeier, L.L. Baxter, R.H. Reeves, Parallels of craniofacial maldevelopment in Down syndrome and Ts65Dn mice, Dev. Dynam. 217 (2000) 137–145.
[36] J. Xiao, A new coordinate system for rodent brain and variability in the brain weights and dimensions of different ages in the naked mole-rat, J. Neurosci. Methods 162 (2007) 162–170.
[37] A. Dorr, J.G. Sled, N. Kabani, Three-dimensional cerebral vasculature of the CBA mouse brain: a magnetic resonance imaging and micro computed tomography study, Neuroimage 35 (2007) 1409–1423.
[38] B. Xiong, et al., Precise cerebral vascular atlas in stereotaxic coordinates of whole mouse brain, Front. Neuroanat. 11 (2017) 128.
[39] M.I. Todorov, et al., Machine learning analysis of whole mouse brain vasculature, Nat. Methods 17 (2020) 442–449.
[40] M. Nouhoum, et al., A functional ultrasound brain GPS for automatic vascular-based neuronavigation, Sci. Rep. 11 (2021) 15197.
[41] C. Brunner, et al., Brain-wide Continuous Functional Ultrasound Imaging for Real-Time Monitoring of Hemodynamics during Ischemic Stroke, 2022, https://doi.org/10.1101/2022.01.19.476904.
[42] A. Urban, et al., Functional ultrasound imaging of cerebral capillaries in rodents and humans, Jacobs Journal of Molecular and Translational Medicine 1 (2015).
[43] K. He, X. Zhang, S. Ren, J. Sun, Deep residual learning for image recognition, in: 2016 *IEEE Conference On Computer Vision And Pattern Recognition (CVPR)* 770–778, IEEE, 2016.
[44] G. Huang, Z. Liu, L. Van Der Maaten, K.Q. Weinberger, Densely connected convolutional networks, in: 2017 IEEE Conference on Computer Vision and Pattern Recognition (CVPR), IEEE, 2017, https://doi.org/10.1109/cvpr.2017.243.
[45] K. Simonyan, A. Zisserman, Very Deep Convolutional Networks for Large-Scale Image Recognition, 2014 *arXiv [cs.CV]*.
[46] A. Dosovitskiy, et al., An Image Is Worth 16x16 Words: Transformers for Image Recognition at Scale, 2020 *arXiv [cs.CV]*.
[47] M. Tan, Q.V. Le, EfficientNetV2: Smaller Models and Faster Training, 2021, https://doi.org/10.48550/arXiv.2104.00298 *arXiv [cs.CV]*.
[48] N. Dalal, B. Triggs, Histograms of oriented gradients for human detection, in: 2005 IEEE Computer Society Conference on Computer Vision and Pattern Recognition (CVPR'05), IEEE, 2005, https://doi.org/10.1109/cvpr.2005.177.
[49] D.G. Lowe, Distinctive image features from scale-invariant keypoints, Int. J. Comput. Vis. 60 (2004) 91–110.
[50] J. Zhang, M. Marszałek, S. Lazebnik, C. Schmid, Local features and kernels for classification of texture and object categories: a comprehensive study, Int. J. Comput. Vis. 73 (2007) 213–238.
[51] J. Deng, et al., ImageNet: a large-scale hierarchical image database, in: 2009 IEEE Conference on Computer Vision and Pattern Recognition, IEEE, 2009, https://doi.org/10.1109/cvpr.2009.5206848.
[52] N. Tajbakhsh, et al., Convolutional neural networks for medical image analysis: full training or fine tuning? IEEE Trans. Med. Imag. 35 (2016) 1299–1312.
[53] J. Adebayo, et al., Sanity Checks for Saliency Maps, 2018 *arXiv [cs.CV]*.
[54] Q. McNEMAR, Note on the sampling error of the difference between correlated proportions or percentages, Psychometrika 12 (1947) 153–157.
[55] R.R. Selvaraju, et al., Grad-CAM: visual explanations from deep networks via gradient-based localization, in: 2017 IEEE International Conference on Computer Vision (ICCV), IEEE, 2017, https://doi.org/10.1109/iccv.2017.74.
[56] R. Geirhos, et al., ImageNet-trained CNNs Are Biased towards Texture; Increasing Shape Bias Improves Accuracy and Robustness, 2018 *arXiv [cs.CV]*.
[57] A. Bar-Zion, et al., Doppler slicing for ultrasound super-resolution without contrast agents, bioRxiv (2021), https://doi.org/10.1101/2021.11.19.469083.
[58] M. Imbault, et al., Functional ultrasound imaging of the human brain activity: an intraoperative pilot study for cortical functional mapping, in: 2016 IEEE International Ultrasonics Symposium (IUS), IEEE, 2016, https://doi.org/10.1109/ultsym.2016.7728505.
[59] M. Imbault, D. Chauvet, J.-L. Gennisson, L. Capelle, M. Tanter, Intraoperative functional ultrasound imaging of human brain activity, Sci. Rep. 7 (2017) 7304.